

Different Mechanisms of Arctic and Antarctic Sea Ice Response to Ocean Heat Transport

Jake Robert Aylmer (✉ j.r.aylmer@pgr.reading.ac.uk)

University of Reading

David Ferreira

University of Reading

Daniel Feltham

University of Reading

Research Article

Keywords: sea ice , ocean heat transport , multidecadal variability , climate models

Posted Date: July 1st, 2021

DOI: <https://doi.org/10.21203/rs.3.rs-637238/v1>

License: © ⓘ This work is licensed under a Creative Commons Attribution 4.0 International License.

[Read Full License](#)

Version of Record: A version of this preprint was published at Climate Dynamics on January 10th, 2022.
See the published version at <https://doi.org/10.1007/s00382-021-06131-x>.



1 Different mechanisms of Arctic and Antarctic sea ice response 2 to ocean heat transport

3 Jake Aylmer · David Ferreira · Daniel Feltham

4
5 Received: [date] / Accepted: [date]

6 **Abstract** Understanding drivers of Arctic and Antarctic sea ice on multidecadal timescales
7 is key to reducing uncertainties in long-term climate projections. Here we investigate the
8 impact of Ocean Heat Transport (OHT) on sea ice, using pre-industrial control simulations
9 of 20 models participating in the latest Coupled Model Intercomparison Project (CMIP6).
10 In all models and in both hemispheres, sea ice extent is negatively correlated with poleward
11 OHT. However, the similarity of the correlations in both hemispheres hides radically different
12 underlying mechanisms. In the northern hemisphere, positive OHT anomalies primarily
13 result in increased ocean heat convergence along the Atlantic sea ice edge, where most of
14 the ice loss occurs. Such strong, localised heat fluxes ($\sim 100 \text{ W m}^{-2}$) also drive increased
15 atmospheric moist-static energy convergence at higher latitudes, resulting in a pan-Arctic
16 reduction in sea ice thickness. In the southern hemisphere, increased OHT is released relatively
17 uniformly under the Antarctic ice pack, so that associated sea ice loss is driven by
18 basal melt with no direct atmospheric role. These results are qualitatively robust across
19 models and strengthen the case for a substantial contribution of ocean forcing to sea ice
20 uncertainty, and biases relative to observations, in climate models.

21 **Keywords** sea ice · ocean heat transport · multidecadal variability · climate models

22 1 Introduction

23 The observed declining trend in Arctic sea ice extent over recent decades is well documented,
24 with significant attribution to anthropogenic climate change (Notz and Marotzke,
25 2012). Antarctic sea ice has slowly expanded over the same period, where the underlying

Jake Aylmer
Department of Meteorology, University of Reading, UK
E-mail: j.r.aylmer@pgr.reading.ac.uk

David Ferreira
Department of Meteorology, University of Reading, UK

Daniel Feltham
Centre for Polar Observation and Modelling, University of Reading, UK

26 processes are not fully understood (Parkinson, 2019). Sea ice plays an important and interac-
27 tive role in climate (Budikova, 2009; Simpkins et al., 2012), impacts human and biological
28 activity (Meier et al., 2014; Convey and Peck, 2019), and is thus an essential metric of cli-
29 mate change. We rely on coupled General Circulation Models (GCMs) to understand the
30 long-term evolution of climate and inform environmental policy. Yet, models participating
31 in the latest (sixth) phase of the Coupled Model Intercomparison Project (CMIP6) simu-
32 late substantially different Arctic sea ice extents, underestimating the observed trend and
33 exhibiting large intermodel spread in projections of its further decline (Notz and SIMIP
34 Community, 2020). There also remain large errors in the simulation of Antarctic sea ice,
35 and most CMIP6 models have decreasing ice extent under historical forcing (Roach et al.,
36 2020). To understand (and ideally reduce) uncertainties and biases against observations, an
37 assessment of the large-scale drivers of sea ice on decadal and longer timescales is required.

38 Previous work has directly examined the impact of OHT on sea ice extent, providing
39 extensive evidence of the former’s influence on the latter. In previous phases of the CMIP,
40 models simulating larger OHTs into the Arctic tend to also simulate larger Arctic ampli-
41 fication and smaller sea ice extent (Mahlstein and Knutti, 2011; Nummelin et al., 2017).
42 Investigations using GCMs have demonstrated anticorrelation of sea ice extent with OHT
43 occurring in simulations with increasing CO₂ emissions (Bitz et al., 2005; Koenigk and
44 Brodeau, 2014; Singh et al., 2017; Auclair and Tremblay, 2018). Some studies manually
45 adjust OHT in GCMs to assess the climate impact: Winton (2003) find a major sea ice
46 retreat when artificially doubling OHT despite concurrent reductions in atmospheric heat
47 transport (AHT). More recently, Docquier et al. (2021) run perturbed northern-hemisphere
48 sea-surface temperature experiments in a CMIP6 model, finding reductions in sea ice extent
49 proportional with the perturbation occurring via basal melt. Others have shown that systems
50 with exotically extensive ice caps (e.g. in the mid-latitudes, as relevant to studies of pre-
51 historic climates) owe their stability to OHT Convergence (OHTC) preventing runaway ice
52 expansion (Poulsen and Jacob, 2004; Ferreira et al., 2011; Rose, 2015; Ferreira et al., 2018).
53 Analytic energy-balance models have shed further theoretical insight, such as how the spa-
54 tial structure of OHT places a limit on sea ice expansion (Rose and Marshall, 2009; Rose,
55 2015) and factors determining how sensitive sea ice is to changes in OHT (Eisenman, 2012;
56 Aylmer et al., 2020).

57 To better understand what role the ocean might play in sea ice uncertainties in models,
58 an evaluation of the relationship between the ocean and sea ice in the latest generation of
59 models is required. Many previous studies analysing the impact of OHT on sea ice have used
60 sensitivity experiments or rely on rising-emission simulations, and frequently emphasis is
61 placed on the Arctic. As such, these describe a forced response of sea ice to OHT, which
62 is indirect in the case of global-warming experiments. In this paper, we instead study the
63 unforced multidecadal variability of both Arctic and Antarctic sea ice cover as simulated by
64 CMIP6 models. The aim is to better understand the means to which such variability is driven
65 by OHT, and how consistently this is exhibited by different models. We focus on large-scale,
66 long-term mean climate metrics to broadly describe and explain model behaviour without
67 explaining the detailed causes of variations in OHT. Practically, this enables a relatively
68 large sample of models to be analysed, providing an indication of the robustness of our
69 results.

70 In section 2, we state the CMIP6 models and simulations used, and briefly describe diag-
71 nostic procedures. As a first step, section 3.1 presents a correlation analysis, which confirms
72 that the strong relation between sea ice extent and OHT remains in CMIP6, while the latitu-
73 dinal dependence of the correlations hints at different behaviours of Arctic and Antarctic sea
74 ice. In section 3.2, using one model, we look in more detail at the spatial variation in ocean

75 and atmospheric heat fluxes to clarify the behaviour underlying those correlations (section
76 3.2). Next, in section 3.3, we demonstrate that our interpretation is broadly robust across our
77 sample of models using simple diagnostics characterising the behaviour of each hemisphere.
78 Finally, in section 4, we summarise and discuss the implications of our results.

79 2 Data and methods

80 2.1 Models and simulations

81 The CMIP6 pre-industrial (PI) control runs provide a set of multi-century simulations of
82 unforced climate variability suitable for this analysis. All models providing the raw fields
83 needed to calculate the main diagnostics required (section 2.2) are included. This gives 20
84 models from various modeling groups, with a range of physical cores and resolutions. Eleven
85 provide a 500 yr time series, one is shorter (CNRM-CM6-1-HR, 300 yr), and the remaining
86 seven are longer (Table 1). Most models have one PI control ensemble member. For MPI-
87 ESM1-2-LR and MRI-ESM2-0, which provide more than one, the longest time series is
88 used (both having realisation label $r = 1$). For CanESM5 and CanESM5-CanOE, we use the
89 member with perturbed-physics label $p = 2$, which uses a different interpolation procedure
90 in coupling wind stress from the atmosphere to the ocean. The developers explain that this
91 improves the representation of local ocean dynamics but otherwise does not substantially
92 impact the large-scale climate relative to the standard configuration with $p = 1$ (Swart et al.,
93 2019). We use the first 1000 yr of the 2000 yr IPSL-CM6A-LR simulation with initialisation
94 label $i = 1$ (because some sections of data were missing for some fields). NorCPM1 provides
95 three 500 yr realisations, but we only analyse $r = 1$. For further details, see the references
96 cited in Table 1.

Table 1 Metadata of the CMIP6 models analysed in this study: lengths of PI-control simulations (t), physical models and approximate resolutions of the atmosphere, ocean, and sea ice components, and references for full details. In each case, sea ice is on the ocean grid

Model	t [yr]	Atmosphere		Ocean	Sea ice	Reference	
ACCESS-CM2	500	MetUM GA7.1	250 km	MOM5	1°	CICE 5.1.2	Bi et al. (2020)
ACCESS-ESM1-5	900	MetUM GA1	250 km	MOM5	1°	CICE 4.1	Ziehn et al. (2020)
CAMS-CSM1-0	500	ECHAM 5	100 km	MOM4	1°	SIS 1.0	Rong et al. (2018)
CanESM5	1050	CanAM5	500 km	NEMO 3.4.1	1°	LIM 2	Swart et al. (2019)
CanESM5-CanOE	500	CanAM5	500 km	NEMO 3.4.1	1°	LIM 2	Swart et al. (2019)
CESM2	1200	CAM6	100 km	POP2	1°	CICE 5.1	Danabasoglu et al. (2020)
CESM2-FV2	500	CAM6	250 km	POP2	1°	CICE 5.1	Danabasoglu et al. (2020)
CESM2-WACCM	500	WACCM6	100 km	POP2	1°	CICE 5.1	Danabasoglu et al. (2020)
CESM2-WACCM-FV2	500	WACCM6	250 km	POP2	1°	CICE 5.1	Danabasoglu et al. (2020)
CNRM-CM6-1-HR	300	ARPEGE 6.3	100 km	NEMO 3.6	0.25°	GELATO 6.1	Voldoire et al. (2019)
CNRM-ESM2-1	500	ARPEGE 6.3	150 km	NEMO 3.6	1°	GELATO 6.1	Séférian et al. (2019)
HadGEM3-GC31-LL	500	MetUM GA7.1	250 km	NEMO 3.6	1°	CICE 5.1	Menary et al. (2018)
HadGEM3-GC31-MM	500	MetUM GA7.1	100 km	NEMO 3.6	0.25°	CICE 5.1	Menary et al. (2018)
IPSL-CM6A-LR	1000	LMDZ 6	250 km	NEMO 3.6	1°	LIM 3	Boucher et al. (2020)
MPI-ESM-1-2-HAM	780	ECHAM 6.3	250 km	MPIOM 1.63	1.5°	In ocean model	Mauritsen et al. (2019)
MPI-ESM1-2-HR	500	ECHAM 6.3	100 km	MPIOM 1.63	0.4°	In ocean model	Müller et al. (2018)
MPI-ESM1-2-LR	1000	ECHAM 6.3	250 km	MPIOM 1.63	1.5°	In ocean model	Mauritsen et al. (2019)
MRI-ESM2-0	700	MRI-AGCM3.5	100 km	MRI-COM 4.4	0.5°	In ocean model	Yukimoto et al. (2019)
NorCPM1	500	CAM-OSLO4.1	250 km	MICOM 1.1	1°	CICE 4	Counillon et al. (2016)
UKESM1-0-LL	1880	MetUM GA7.1	250 km	NEMO 3.6	1°	CICE 5.1	Sellar et al. (2019)

97 2.2 Diagnostics

98 *Sea ice* Sea ice extent, S_i , is calculated directly from the monthly sea ice concentration, c_i ,
 99 and ocean grid cell area, a_o , fields by summing a_o over cells with $c_i \geq c_i^*$, in each hemisphere
 100 separately, as a function of time. The concentration threshold, c_i^* , is taken to be 15%. For
 101 consistency this is done regardless of whether S_i is provided, since the c_i data is required
 102 for other diagnostics, including the latitude of the sea ice edge, ϕ_i . For this, rather than just
 103 using the c_i^* contour, we interpolate c_i onto a regular, fixed grid, then follow the algorithm
 104 described by Eisenman (2010). This determines ϕ_i as a function of longitude by identifying
 105 meridionally adjacent grid cells where the equatorward cell satisfies $c_i < c_i^*$ and the poleward
 106 cell satisfies $c_i \geq c_i^*$. If land is present in the meridionally-nearest n cells to the identified
 107 pair, it is rejected. In the case of multiple ice edges for a given longitude, the one nearest
 108 the equator is chosen. This procedure results in a set of ice edges representative of the
 109 thermodynamically-driven evolution of the sea ice cover, eliminating locations where the ice
 110 edge is temporarily fixed simply because there is no ocean for it to move into. We interpolate
 111 c_i onto a $0.5^\circ \times 0.5^\circ$ grid, and use $n = 2$ which corresponds to about 100 km. Since we are
 112 considering long-term averages, the sensitivity to the choice of interpolation resolution, the
 113 land-checking parameter n , and selecting nearest the pole instead of the equator in the case
 114 of multiple ice edges, is low.

115 The ice edge latitude diagnosed in this way and zonally averaged is an effective way of
 116 quantifying the sea ice cover, because it can be easily compared across models and works
 117 naturally when evaluating heat transported across a fixed latitude (as in Fig. 1). The two
 118 metrics, S_i and ϕ_i , are strongly related in each model (Online Resource 1, Fig. S1.1), and are
 119 thus effectively interchangeable; i.e. conclusions based on ϕ_i can be applied to S_i (with sign
 120 reversal).

121 For sea ice thickness, H_i , we take the ‘sivol’ field, which is the ice volume per unit cell
 122 area, and divide by c_i to get the actual floe thickness. We could not produce H_i for CanESM5,
 123 CanESM5-CanOE, or NorCPM1 because ‘sivol’ was not provided.

124 *Meridional heat transport* At the time of analysis, few models provided northward OHT
 125 already diagnosed (CMIP6 variable name: ‘hfbasin’). Computing OHT directly from the
 126 ocean current and temperature fields for each model is impractical due to data volume, non-
 127 trivial grid geometries, and issues with closing heat budgets which may be worsened by
 128 interpolation. Most models provided the net downward energy flux into the top of the ocean
 129 column (‘hfds’). We thus approximate northward OHT at each latitude ϕ by integrating hfds
 130 north of ϕ . This neglects heat storage tendency (also not commonly provided), which on
 131 timescales relevant to this work manifests as a non-zero heat transport at the south pole of
 132 typical magnitude 0.1 PW (Online Resource 1, Fig. S1.2), or less than 1 W m^{-2} averaged
 133 over the world ocean. For the Southern Hemisphere (SH) analysis, we compute a second
 134 version of OHT by starting the integration at the south pole and proceeding north, which
 135 shifts the accumulated error into the Northern Hemisphere (NH).

136 The turbulent, longwave, and shortwave heat fluxes evaluated at the surface and top
 137 of atmosphere are combined to give the net heat flux into the atmospheric column, which,
 138 neglecting atmospheric heat storage, gives the column-integrated moist-static energy con-
 139 vergence. Then Atmospheric Heat Transport (AHT)¹ follows from integrating in a similar
 140 manner as is done for OHT. Although neglecting the heat capacity of the atmosphere is a

¹ We refer to the net atmospheric moist-static energy transport as ‘heat transport’ for symmetry of terminology with OHT.

141 very good approximation, we compute a second version of AHT, integrating from the south
142 pole, for consistency with the OHT calculation.

143 2.3 Time-series analysis

144 To analyse how sea ice responds to natural variations in oceanic and atmospheric heat fluxes
145 during the PI control simulations, we take a simple approach of dividing each time series
146 into consecutive, non-overlapping Δt year averages, and calculating Pearson correlations,
147 r , between each pair of diagnostics. We use $\Delta t = 25$ yr, which is sufficiently long to study
148 multidecadal variability, and each diagnostic is approximately uncorrelated (with itself) on
149 this timescale (Online Resource 1, Fig. S1.3). To give a sense of the significance of r , critical
150 values r_{crit} of a two-tailed Student's t -test on the null hypothesis that $r = 0$, at the 95%
151 confidence level, are computed. Values of r exceeding r_{crit} in magnitude are then significant
152 at the 95% confidence level. These depend on the time series length: for the shortest (300 yr),
153 most common (500 yr), and longest (1880 yr) time series respectively, $r_{\text{crit}} = 0.50, 0.38$, and
154 0.19 .

155 3 Results

156 3.1 Correlations between ϕ_i , OHT, and AHT

157 *Northern hemisphere* We start by computing r between ϕ_i , OHT, and AHT, as a function of
158 the latitude at which the heat transports are evaluated. In the NH, 19 of 20 models show a
159 positive correlation between OHT and ϕ_i equatorward of the ice edge (Fig. 1a, right). This is
160 physically intuitive (increased heat is associated with less sea ice) and consistent with previ-
161 ous studies (section 1). All models have $r > r_{\text{crit}}$ for at least one latitude equatorward of their
162 mean ice edges. In many cases the correlations are strong and do not vary that much with
163 latitude. There is an abrupt change in r poleward of the ice edge, occurring roughly at the
164 seasonal minimum ice extent: some r become quite strongly negative, whereas most (11)
165 drop to an insignificant value. One model, CNRM-ESM2-1, retains a significantly strong
166 positive correlation up to the pole. The same 19 of 20 models have a negative correlation
167 between AHT and ϕ_i equatorward of the ice edge, although there is more variation across
168 models and fewer retain $|r| > r_{\text{crit}}$ up to the ice edge (Fig. 1c, right). Such negative cor-
169 relations are physically non-intuitive, but can be understood as a consequence of Bjerknes
170 compensation. Essentially, Bjerknes (1964) proposed that if the top-of-atmosphere fluxes
171 and total heat content are close to constant, it follows that the total meridional heat trans-
172 port must be fixed. Consequently, increases in OHT should be balanced by the equivalent
173 decrease in AHT (and vice versa). Here, this manifests as a negative correlation between
174 OHT and AHT, present in all models equatorward of the mean ice edge (Fig. 1d, right). For
175 many models, AHT and OHT become uncorrelated over sea ice, which can be attributed
176 to minimal air–sea exchanges necessary for the compensation to occur. As with OHT there
177 is a sharp change in $r(\text{AHT}, \phi_i)$ across the ice edge but, in contrast, all 20 models have
178 significant positive $r(\phi_i, \text{AHT})$ over the permanent ice cover.

179 *Southern hemisphere* The picture in the SH does not mirror that in the NH. There is a large
180 variation in $r(\text{OHT}, \phi_i)$ across models between 50° – 60° S (Fig. 1a, left), with four mod-
181 els having significantly negative $r(\phi_i, \text{OHT})$. Excluding MPI-ESM-1-2-HAM, these corre-
182 lations converge at high positive values near 65° S—roughly at the mean ice edge. When

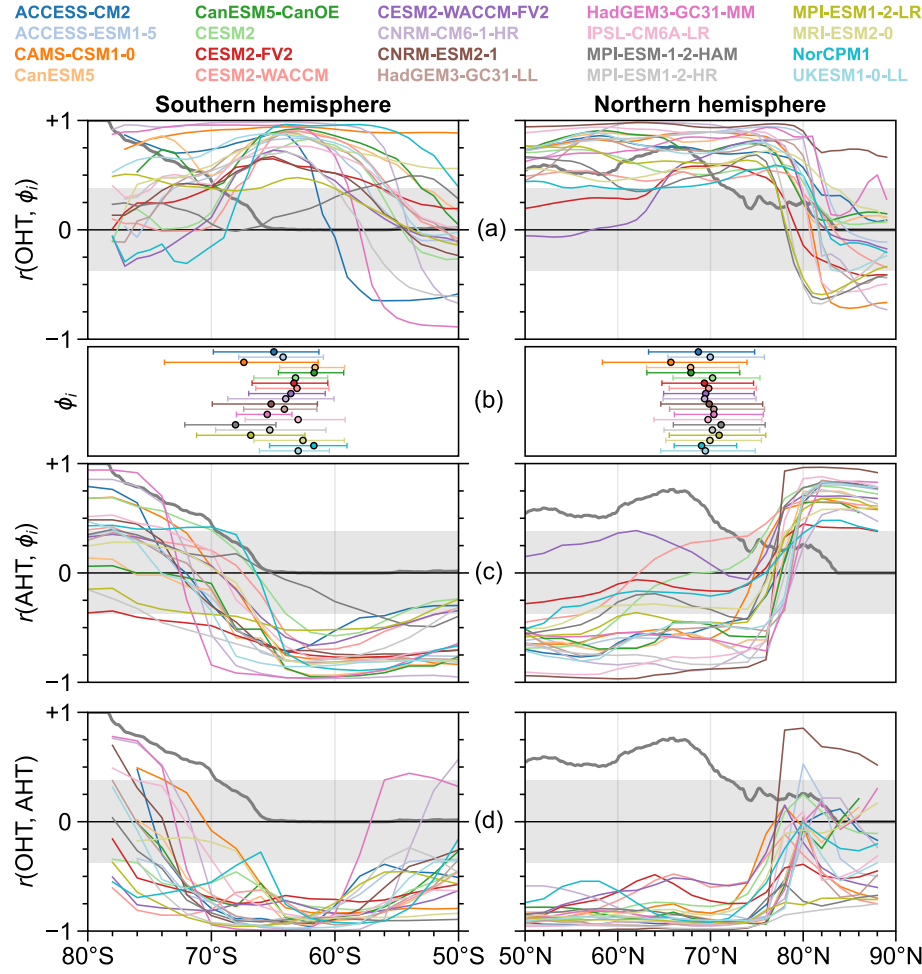


Fig. 1 (a) Correlation (r) between 25 year mean, zonal-mean sea ice edge latitude, ϕ_i , and poleward Ocean Heat Transport (OHT) as a function of latitude in the (left) southern and (right) northern hemispheres. (b) Mean ϕ_i in each model (circles) and seasonal range indicated by the mean September/March values of ϕ_i (horizontal bars). (c) As in (a) but for poleward Atmospheric Heat Transport (AHT). (d) Correlation between OHT and AHT as a function of latitude. Shading indicates where r is insignificant at the 95% confidence level based on a t -test for 500 year time series. Thick grey lines in (a), (c), and (d) show the fraction of longitudes occupied by land at each latitude. Note the reversed horizontal axis in the left panels

183 considering higher southern latitudes, we must bear in mind that the area of enclosed ocean
 184 reduces to zero as the Antarctic coastline is approached, such that the correlations become
 185 less meaningful. This is addressed more directly in the next sections, but for now the left
 186 panels of Fig. 1 show the zonal land fraction as a function of latitude to approximately indi-
 187 cate the location of Antarctica. For all models except MPI-ESM-1-2-HAM, there is at least
 188 one latitude equatorward of its mean ϕ_i which has $r(\text{OHT}, \phi_i) > r_{\text{crit}}$. AHT is significantly
 189 negatively correlated with ϕ_i for most models between 50° – 65°S (Fig. 1c, left). For some,
 190 $r(\text{AHT}, \phi_i)$ becomes significantly positive at higher latitudes, from about 72°S . However,
 191 the land fraction here is above 0.5, so that AHT across these latitudes mostly converges

192 over Antarctica. In contrast, $r(\text{OHT}, \phi_i)$ remains generally positive between ϕ_i and the 0.5
 193 land-fraction latitude. Bjerknes compensation is indicated in the southern hemisphere (Fig.
 194 1d, left), although less strongly than in the NH and two models (CNRM-CM6-1-HR and
 195 HadGEM3-GC31-MM) do not show the signal at the lower latitudes of the range plotted.
 196 All models have significantly strong compensation at about 65°S , coincident with the loca-
 197 tion of strongest $r(\text{OHT}, \phi_i)$.

198 This correlation analysis points toward qualitatively different behaviours of the Arctic
 199 and Antarctic sea ice cover. In both hemispheres, there tends to be less sea ice when pole-
 200 ward OHT increases just equatorward of the ice edge. This holds, roughly, with OHT under
 201 the Antarctic ice pack, which implies that sea ice contracts via increased basal melting.
 202 However, reduced Arctic sea ice cover is associated with increased AHT over the perma-
 203 nent ice pack, where there is no consistent relation with OHT across models, i.e. direct
 204 ocean–ice fluxes do not seem relevant in the NH in most cases. Possible explanations for the
 205 NH correlations are OHT driving AHT Convergence (AHTC) at higher latitudes, causing
 206 melt from above, and/or OHT having a more localised effect by increasing OHTC close to
 207 the ice edge. Such potential mechanisms are not mutually exclusive and could be exhibited
 208 to different degrees across models. To examine this in a more direct and physical way, we
 209 next look at spatial patterns of changes in ocean and atmospheric heat fluxes, and key sea
 210 ice metrics (concentration, thickness, and surface temperature).

211 3.2 Spatial distribution of changes in heat fluxes

212 We compute the change in various diagnostics between two 25 year mean states correspond-
 213 ing to the minimum and maximum mean ϕ_i . Here we focus on one model, HadGEM3-GC31-
 214 LL, which is a typical case and has about the average value and magnitude of variability of
 215 ϕ_i in both hemispheres. This facilitates presentation and overall, we find no major differ-
 216 ences in the qualitative, large-scale behaviour when repeating this procedure on the other
 217 models. In section 3.3, summary statistics of all models are provided (which also assess the
 218 whole time series rather than just the extrema, Tables 2–3) and the set of contour plots for
 219 all 20 models can be found in Online Resource 2.

220 *Northern hemisphere* Most of the change in Arctic sea ice extent occurs in the Atlantic
 221 sector. A concentrated increase in OHTC $\sim 60 \text{ W m}^{-2}$ occurs in the Barents Sea where
 222 ϕ_i retreats by $\sim 2^\circ\text{N}$ (Fig. 2c), coincident with substantial reductions in sea ice concentra-
 223 tion (Fig. 2a) and thickness (Fig. 2b). Comparable poleward shift in ϕ_i also occurs in the
 224 Greenland Sea, but with strong localised OHTC slightly further poleward of the ice edge
 225 compared with the Barents Sea. Between these areas, near Svalbard, is a patch of decreased
 226 OHTC $\sim 20 \text{ W m}^{-2}$, and the change in ϕ_i is about half that in the Barents Sea. Strong OHTC
 227 also occurs in the Labrador Sea where ϕ_i retreats by $\sim 2^\circ\text{N}$, although the change in thickness
 228 is less striking than in the Greenland and Barents Seas. Across the open ocean, ΔAHTC
 229 (Fig. 2d) is approximately the same magnitude as ΔOHTC but of the opposite sign, which
 230 implies the top-of-atmosphere flux does not change much and confirms the presence of
 231 Bjerknes compensation. In the Pacific sector, sea ice expands by a very small amount in the
 232 Bering Sea, contracts by a similarly small amount in the Sea of Okhotsk, and in both cases
 233 the local ΔOHTC and ΔAHTC is small. In sum, ϕ_i retreats more wherever OHTC increases
 234 more.

235 In the central Arctic, OHTC and sea ice concentration barely change, yet the ice thick-
 236 ness decreases by a substantial $\sim 50 \text{ cm}$, similar to the reduction near the Atlantic ice edge

237 where OHTC is strong. Over sea ice, ΔAHTC indicates the sign of the change in net downward
 238 surface flux², which increases over most of the Arctic ice pack. Averaged over sea ice,
 239 the mean change in OHTC is approximately zero while that of AHTC is a few W m^{-2} (this
 240 is quantified in section 3.3 and Fig. 5). Thus the reduction in ice thickness at high latitudes
 241 must be attributed primarily to surface rather than basal melt. This is verified by the surface
 242 air temperature (T_s , Fig. 2e) and downwelling longwave radiation (F_{dn} , Fig. 2f). Both
 243 T_s and F_{dn} increase over most of the Arctic ice pack, skewed towards the Atlantic sector
 244 where OHTC is sufficiently high to both erode the ice edge and promote surface warming.
 245 Since AHT and OHT are highly anticorrelated between 50° – 70°N (Fig. 1d), the increase in
 246 AHTC in the central Arctic must be primarily driven by oceanic heat loss close to the ice
 247 edge. On the other side of the Arctic, a modest increase in ice thickness occurs (~ 30 cm)
 248 in the Chukchi Sea, coincident with slightly reduced T_s and F_{dn} , supporting the notion that
 249 ice thickness changes are surface driven. There is possibly a dynamical component to the
 250 explanation of sea ice changes in the central Arctic; this is beyond the scope of our investigation,
 251 but we speculate the ice thickness changes are likely mostly thermodynamically driven
 252 because of the timescales considered and the apparent spatial correlation of ΔH_i with ΔF_{dn}
 253 and ΔT_s . This interpretation is also reminiscent of Ding et al. (2017), who argue a major
 254 role of strengthening atmospheric circulation on recent summer Arctic sea decline acting,
 255 ultimately, via increased downwelling longwave radiation at high latitudes.

256 The spatial distributions of the changes in these diagnostics are largely the same in the
 257 other 19 models, with only minor exceptions. All models show increased OHTC somewhere
 258 in the vicinity of the Atlantic ice edge of several tens of W m^{-2} , and only a few have simi-
 259 larly high values in the Pacific sector. In CNRM-ESM2-1, ΔOHTC reaches 150 W m^{-2}
 260 in the Greenland sea where the ice edge retreats by about 5°N . CanESM5 and CanESM5-
 261 CanOE stand out as having relatively extensive ice cover in the Denmark Strait, in which
 262 OHT converges nearer the coast of Greenland (i.e. well under sea ice). High-latitude ice
 263 thickness decreases by several tens of centimeters in all models, even in cases with mod-
 264 est variations in overall sea ice extent (e.g. CESM2 which only has strong ΔOHTC in the
 265 Labrador sea). As in HadGEM3-GC31-LL, many models have some areas of increased H_i ,
 266 usually in the Pacific sector. Reduction in sea ice concentration is always localised near the
 267 ice edge; in a few models the sea ice concentration increases by a few percent in the central
 268 Arctic. These results strongly suggest that, on multidecadal timescales, variations in Arctic
 269 sea ice extent are primarily driven by local OHT convergence causing the ice edge to retreat
 270 in the vicinity. This has a secondary effect of enhancing AHT into higher latitudes where
 271 the ice volume decreases [explaining the change in sign of $r(\text{AHT}, \phi_i)$ across the summer
 272 (i.e. perennial) ice edge in Fig. 1c].

273 *Southern hemisphere* Like in the Arctic, the largest reductions in Antarctic sea ice extent
 274 occur where the largest increases in OHTC occur: for HadGEM3-GC31-LL, this is primarily
 275 in the Ross Sea (Fig. 3c). The difference is that OHTC increases by several W m^{-2} at most
 276 longitudes and well under the Antarctic ice pack. Consequently, the reduction in sea ice
 277 concentration and thickness (Figs. 3a–b) is relatively spatially uniform; although the largest
 278 reductions in c_i and H_i do occur in the Ross Sea. There are a few regional exceptions: in the
 279 Amundsen-Bellinghousen Sea, ΔOHTC is smaller and the ice edge does not move much;
 280 and decreased OHTC at about 110° – 120°E coincides with slight ice expansion.

² We plotted the actual net downward surface flux to verify this but do not include it because it is almost identical to Fig. 2d. This is also the case in the southern hemisphere.

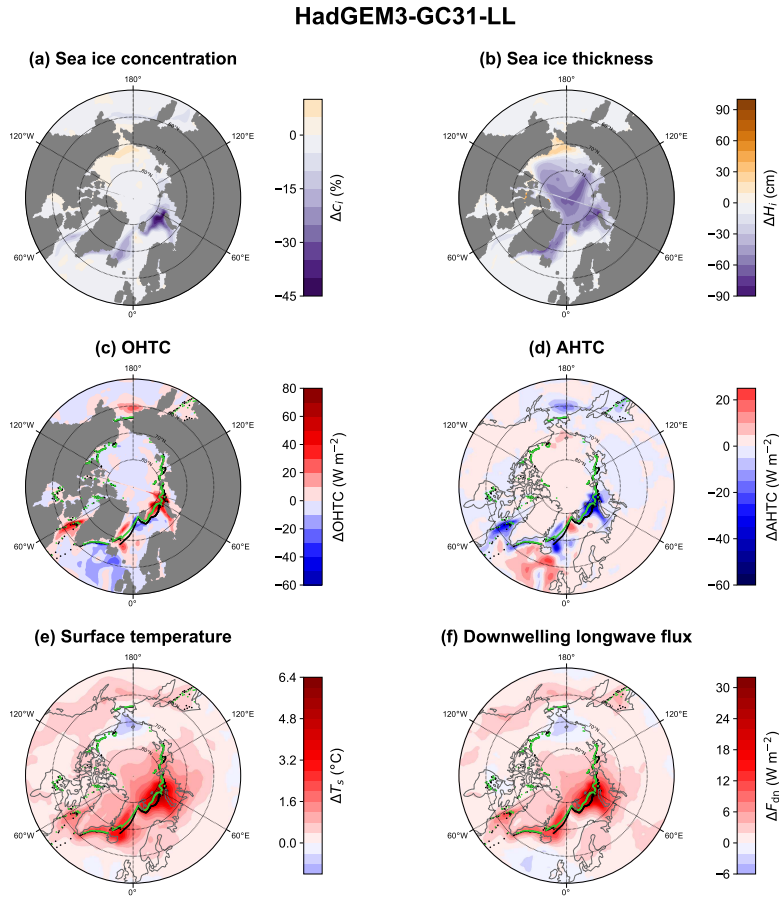


Fig. 2 Change in (a) sea ice concentration, c_i , (b) sea ice thickness, H_i , (c) OHT convergence, (d) AHT convergence, (e) surface air temperature, T_s , and (f) downwelling longwave radiation, F_{dn} , between the maximum (black) and minimum (green) 25 year mean Arctic sea ice extent in HadGEM3-GC31-LL. Note that there are ≤ 1 ice-edge points per longitude (see section 2.2)

281 Figure 3d shows that ΔAHTC is approximately the same magnitude but opposite sign
 282 to ΔOHTC (as seen in the Arctic), but in the Antarctic this is true over sea ice as well as
 283 open ocean. This can be attributed to the lower mean sea ice concentration (43% in the
 284 Antarctic compared to 70% in the Arctic at maximum sea ice extent in HadGEM3-GC31-
 285 LL), such that air–sea exchanges are significantly less inhibited. Figure 3e–f show that T_s
 286 and F_{dn} increase quite uniformly over sea ice, with the largest increases roughly coinciding
 287 with the largest increases in OHTC. Over Antarctica, T_s , F_{dn} , and AHTC do not change
 288 that much. Thus the increased surface warming and downwelling longwave radiation are an
 289 effect of OHTC but are not attributed to the loss of ice thickness or concentration, because
 290 the net surface flux (roughly, AHTC) decreases (which, by itself, would have a surface
 291 cooling effect). Figure 3c clearly shows heat being transported under sea ice, and explains
 292 why $r(\text{OHT}, \phi_i)$ is largest with OHT evaluated near to the ice edge (Fig. 1a).

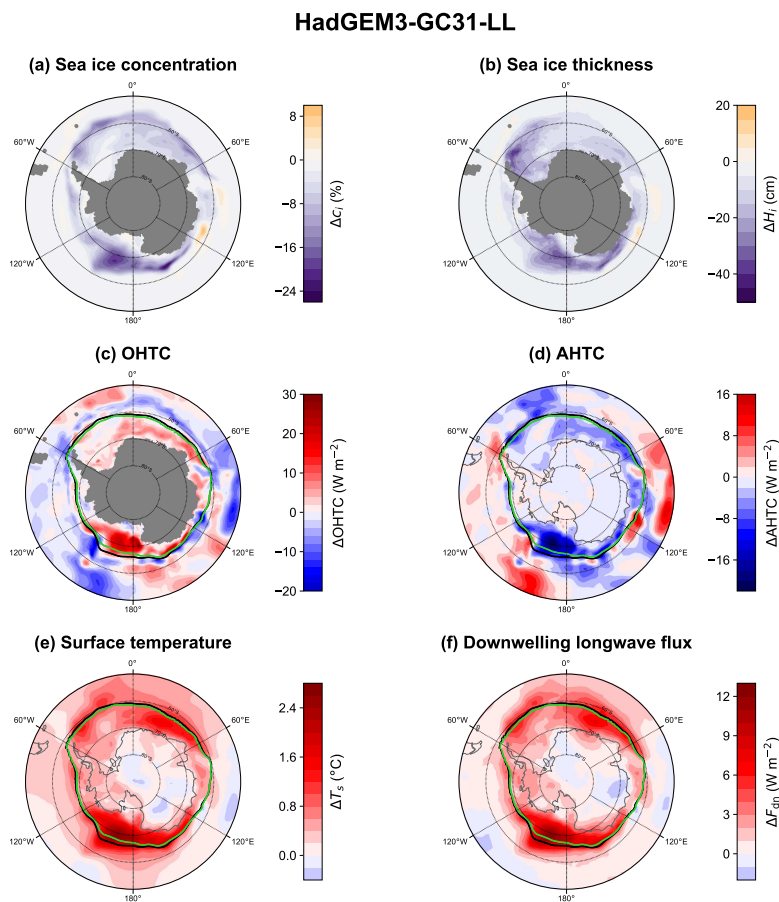


Fig. 3 As in Fig. 2 but for the southern hemisphere

293 All models show the same basic features as HadGEM3-GC31-LL: OHTC broadly in-
 294 creases under the Antarctic ice pack, $\Delta AHTC$ is roughly the same but with opposite sign,
 295 and T_s increases most wherever OHTC is largest. Although the increase in OHTC is fairly
 296 spatially uniform (compared to the NH), roughly half of models have the largest $\Delta OHTC$
 297 in the Ross Sea, while for the others it occurs in the Weddell Sea. CNRM-CM6-1-HR, with
 298 the largest variation in Antarctic sea ice extent, exhibits strong $\Delta OHTC \sim 40 W m^{-2}$ in the
 299 Weddell Sea where the ice edge retreats by $\sim 8^{\circ}S$. NorCPM1 is slightly unusual in that most
 300 of its strong increase in OHTC is concentrated closer to the ice edge in the Amundsen Sea,
 301 Ross Sea, and East Antarctica, such that the behaviour looks more like that in the NH. Its
 302 mean sea ice concentration (42%) is comparable to that in HadGEM3-GC31-LL. However,
 303 there is still clearly non-zero OHTC increase under the ice, particularly in the Weddell Sea
 304 ($\sim 10 W m^{-2}$). CESM2-WACCM-FV2 has the smallest variation in Antarctic sea ice extent,
 305 and it has small changes in both OHTC and AHTC even though the ice concentration and
 306 thickness vary by similar amounts to HadGEM3-GC31-LL. This is possibly indicative of a
 307 higher intrinsic sensitivity in this model.

308 3.3 Heat fluxes averaged over sea ice

309 In the previous section, we showed the changes in various heat fluxes in HadGEM3-GC31-
 310 LL as the system moved from the minimum to maximum sea ice cover during the PI control
 311 simulation. This is useful for illustration but only shows the extrema—is our interpretation
 312 valid for the whole time series? To check this, we require diagnostics that quantify the in-
 313 ferred mechanisms. Specifically, we suggested that most of the positive anomalies in OHT
 314 are lost near the ice edge in the NH, while most converges under sea ice in the SH. Con-
 315 currently, AHTC increases (decreases) over sea ice in the NH (SH). Let h_o (h_a) be OHTC
 316 (AHTC) averaged under (over) the ice pack. For h_o this is computed by simply averaging the
 317 hfds field over grid cells where $c_i \geq c_i^*$. A similar procedure is done h_a , but including the net
 318 flux into the atmospheric column and interpolating c_i onto the atmospheric grid (see section
 319 2.2). Since c_i varies with time, the averages h_o and h_a themselves follow changes in sea ice.
 320 These also conveniently eliminate land-covered points from AHTC and zonal asymmetries.
 321 The annual series of h_o and h_a are then converted to series of 25 year averages in the same
 322 way as the previous diagnostics, and correlations between those and ϕ_i are computed.

323 *Northern hemisphere* The correlations $r(h_o, \phi_i)$ and $r(h_a, \phi_i)$ in the NH (Table 2a,b) largely
 324 confirm what is suggested by Fig. 1 and are consistent with our discussion in section 3.2.
 325 All models have $r(h_a, \phi_i) > 0$, although two (CanESM5-CanOE and CNRM-CM6-1-HR) are
 326 statistically insignificant. The correlation of ϕ_i with h_o varies across models: four have strong
 327 positive $r(h_o, \phi_i)$, and a few (notably all CESM models) have strong negative $r(h_o, \phi_i)$. The
 328 ones with strong positive $r(h_o, \phi_i)$ are those which have more extensive ice in the Denmark
 329 Strait/Labrador Sea area (both CanESM models) or have larger overall variations (CNRM-
 330 ESM2-1), such that h_o captures the direct effect of OHTC. In contrast, all but two models
 331 have statistically significant positive $r(h_a, \phi_i)$. Most have $r(\text{OHT}, h_a) > 0$, suggesting that
 332 the increase in AHTC over sea ice is at least partly ocean driven, but many are relatively
 333 weak (Table 2b). The reduced correlation between OHT and h_a could be attributed to the
 334 reduction in AHT as OHT increases, such that there are two competing influences on h_a :
 335 (i) the overall decrease in heat available from AHT and (ii) the increase in heat available
 336 from ocean heat loss near the ice edge. In Table 2c we include correlations with f_{dn} , the
 337 downwelling longwave flux averaged over sea ice, computing f_{dn} in an analogous proce-
 338 dure to h_a . All models have significant positive $r(f_{\text{dn}}, \phi_i)$, and most have significant positive
 339 $r(\text{OHT}, f_{\text{dn}})$ (Table 2c). This supports the atmosphere acting as a ‘bridge’ connecting in-
 340 coming OHT to the top ice surface. From a more general perspective, surface warming is
 341 associated with both loss of sea ice and and increased OHT (Table 2d). Studies have al-
 342 ready shown a relation between global mean surface temperature and sea ice extent in both
 343 hemispheres (e.g. Rosenblum and Eisenman, 2017). Given the correlations between OHT,
 344 T_s , and ϕ_i , our results imply a potential role of OHT in explaining model differences in such
 345 relationships.

Table 2 Northern hemisphere correlations for various diagnostics. The first two columns list the latitude, ϕ_0 ($^{\circ}$ N), where the maximum correlation between OHT and ϕ_i occurs and the corresponding value. (a)–(d) list correlations of the stated diagnostic with (left) OHT, and with (right) ϕ_i . (a) OHT convergence averaged over sea ice, h_o . (b) AHT convergence averaged over sea ice, h_a . (c) Downwelling longwave radiation averaged over sea ice, f_{dn} . (d) Surface air temperature averaged over ϕ_0 – 90° N, T_s . Values in bold are statistically significant at the 95% confidence level. Cells are shaded on a red (+1) through white (0) to blue (–1) color scale as a visual aid

Model	max $r(\text{OHT}, \phi_i)$		(a) h_o		(b) h_a		(c) f_{dn}		(d) T_s	
	ϕ_0	r	r_{OHT}	r_{ϕ_i}	r_{OHT}	r_{ϕ_i}	r_{OHT}	r_{ϕ_i}	r_{OHT}	r_{ϕ_i}
ACCESS-CM2	58	+0.86	+0.67	+0.30	+0.28	+0.63	+0.42	+0.72	+0.71	+0.92
ACCESS-ESM1-5	69	+0.94	–0.03	–0.35	+0.58	+0.82	+0.63	+0.72	+0.86	+0.93
CAMS-CSM1-0	65	+0.89	+0.18	–0.02	+0.07	+0.40	+0.52	+0.50	+0.81	+0.88
CanESM5	59	+0.88	+0.79	+0.67	+0.32	+0.46	+0.50	+0.62	+0.78	+0.88
CanESM5-CanOE	58	+0.91	+0.88	+0.72	+0.16	+0.35	+0.52	+0.55	+0.78	+0.86
CESM2	55	+0.73	–0.43	–0.85	+0.45	+0.73	+0.58	+0.86	+0.75	+0.95
CESM2-FV2	69	+0.59	–0.26	–0.76	–0.18	+0.41	+0.15	+0.61	+0.41	+0.87
CESM2-WACCM	56	+0.55	–0.30	–0.82	+0.38	+0.83	+0.30	+0.68	+0.57	+0.91
CESM2-WACCM-FV2	69	+0.82	–0.06	–0.61	+0.00	+0.63	+0.33	+0.84	+0.52	+0.95
CNRM-CM6-1-HR	62	+0.98	+0.56	+0.53	+0.36	+0.40	+0.65	+0.66	+0.85	+0.86
CNRM-ESM2-1	62	+0.98	+0.69	+0.68	+0.91	+0.92	+0.92	+0.95	+0.97	+0.99
HadGEM3-GC31-LL	58	+0.84	+0.21	–0.13	+0.36	+0.64	+0.63	+0.73	+0.84	+0.96
HadGEM3-GC31-MM	68	+0.94	+0.10	–0.35	+0.44	+0.81	+0.71	+0.87	+0.82	+0.97
IPSL-CM6A-LR	58	+0.94	–0.32	–0.27	+0.91	+0.92	+0.82	+0.91	+0.94	+0.98
MPI-ESM1-2-HAM	50	+0.69	–0.09	–0.55	+0.36	+0.78	+0.29	+0.75	+0.60	+0.89
MPI-ESM1-2-HR	70	+0.90	+0.09	–0.21	+0.27	+0.61	+0.60	+0.77	+0.85	+0.96
MPI-ESM1-2-LR	51	+0.77	–0.29	–0.46	+0.48	+0.77	+0.58	+0.66	+0.70	+0.87
MRI-ESM2-0	69	+0.72	+0.52	–0.05	+0.08	+0.65	+0.36	+0.70	+0.56	+0.90
NorCPM1	51	+0.59	+0.43	–0.20	–0.08	+0.47	+0.19	+0.49	+0.48	+0.74
UKESM1-0-LL	57	+0.89	+0.30	+0.12	+0.55	+0.69	+0.56	+0.76	+0.82	+0.94

346 *Southern hemisphere* Thirteen models exhibit strong (> 0.7) positive correlation of ϕ_i with
 347 h_o and correspondingly strong negative correlation with h_a , confirming again the description
 348 in section 3.2 (Table 3). Some models do not fit this, including all CESM models: CESM2 is
 349 the only model to show a significant (although weak) negative $r(h_o, \phi_i)$ despite having sig-
 350 nificantly positive $r(\text{OHT}, \phi_i)$, while the other CESM models show statistically-insignificant
 351 $r(h_o, \phi_i)$. These models have among the smallest variance in h_o and ϕ_i , so the signal-to-noise
 352 ratio could be too small to draw a meaningful interpretation in these cases (or the Antarctic
 353 sea ice sensitivity to OHT is relatively small). CAMS-CSM1-0 has practically no correla-
 354 tion between h_o and ϕ_i , despite strong positive $r(\text{OHT}, \phi_i) > 0.75$ up to the Antarctic coast.
 355 However, this model has cancelling regions of positive and negative OHTC under ice in the
 356 Weddell Sea (Online Resource 2, Fig. S2.6) and h_o averages over both regions. Similar reason-
 357 ing explains the small $r(h_o, \phi_i)$ and $r(h_a, \phi_i)$ in MPI-ESM-1-2-HAM (Online Resource
 358 2, Fig. S2.28), which also has the smallest mean Antarctic sea ice extent (Fig. 1b). The fact
 359 that Bjerknes compensation is maintained over much of the Antarctic sea ice pack (Fig. 1d,
 360 left), suggests that the negative correlation between ϕ_i and h_a mostly reflects heat loss from
 361 the ocean into the atmosphere via leads. There could be a negative feedback such that the
 362 resulting AHT divergence offsets the effect of OHT convergence, however it is difficult to
 363 ascertain this in the present analysis.

364 Comparing Tables 2 and 3, columns (a)–(b), emphasises the broad hemispheric asym-
 365 metry in the response of ϕ_i to h_o and h_a . To illustrate this further, we compute $\Delta\phi_i$ as the
 366 difference between the maximum and minimum ϕ_i (from the 25 year averages), and ΔD
 367 as the difference in diagnostic D between the same times at which $\max(\phi_i)$ and $\min(\phi_i)$
 368 occur—exactly as was done for Figs. 2–3. While $\Delta\phi_i$ could loosely be interpreted as a
 369 ‘signed standard deviation’, our aim with this is just to concisely summarise the general
 370 qualitative conclusions. This metric is conducive to this end, as it gives single data points
 371 per model, eliminates differences in mean states, and retains the sign of the relationship
 372 between variables. Figure 4 shows that models with larger increases in ϕ_i are associated
 373 with larger increases (decreases) in poleward OHT (AHT) in both hemispheres (matching
 374 individual model descriptions). Figure 5 shows that h_o does not change much between the
 375 maximum and minimum sea ice states across models in the NH, but that h_o increases by
 376 a few W m^{-2} in the SH. In all models, h_a increases from the minimum to maximum ϕ_i
 377 in the NH, but decreases in the SH. The analysis in section 3.2 suggests that, in the SH, h_a
 378 decreases in response to Bjerknes compensation (which does not occur in the NH because
 379 the ice concentration is too high). Figure 6 reinforces our earlier point that the OHT–sea
 380 ice relationships revealed here could be in part responsible for the previously noted relation
 381 between sea ice extent and surface temperature. It is worth noting the non-zero intercepts of
 382 the fitted linear relations between $\Delta\phi_i$ and the other diagnostics in Figs. 4–6. This indicates
 383 that the variability of ϕ_i cannot be wholly attributed to anomalies in heat transports.

Table 3 As in Table 2 but for the southern hemisphere, and here ϕ_i and ϕ_0 are in $^{\circ}\text{S}$

Model	max $r(\text{OHT}, \phi_i)$		(a) h_o		(b) h_a		(c) f_{dn}		(d) T_s	
	ϕ_0	r	r_{OHT}	r_{ϕ_i}	r_{OHT}	r_{ϕ_i}	r_{OHT}	r_{ϕ_i}	r_{OHT}	r_{ϕ_i}
ACCESS-CM2	64	+0.88	+0.87	+0.90	-0.87	-0.85	+0.61	+0.73	+0.83	+0.97
ACCESS-ESM1-5	63	+0.84	+0.79	+0.79	-0.47	-0.49	+0.26	+0.11	+0.82	+0.87
CAMS-CSM1-0	64	+0.94	-0.10	+0.02	-0.38	-0.47	+0.50	+0.58	+0.91	+0.92
CanESM5	61	+0.90	+0.79	+0.91	-0.64	-0.76	+0.22	+0.43	+0.80	+0.93
CanESM5-CanOE	61	+0.92	+0.77	+0.91	-0.55	-0.71	+0.19	+0.32	+0.84	+0.93
CESM2	62	+0.83	-0.13	-0.48	-0.64	-0.57	+0.46	+0.71	+0.73	+0.97
CESM2-FV2	63	+0.65	+0.74	+0.26	-0.48	-0.72	+0.13	+0.20	+0.26	+0.72
CESM2-WACCM	63	+0.90	+0.04	-0.17	-0.55	-0.42	+0.40	+0.62	+0.67	+0.89
CESM2-WACCM-FV2	63	+0.73	+0.24	-0.29	-0.53	-0.60	+0.17	+0.24	+0.42	+0.91
CNRM-CM6-1-HR	63	+0.99	+0.97	+0.98	-0.86	-0.86	+0.79	+0.82	+0.97	+0.99
CNRM-ESM2-1	65	+0.67	+0.70	+0.85	-0.46	-0.79	+0.64	+0.44	+0.78	+0.72
HadGEM3-GC31-LL	64	+0.89	+0.88	+0.76	-0.75	-0.57	+0.54	+0.71	+0.70	+0.89
HadGEM3-GC31-MM	64	+0.96	+0.95	+0.95	-0.87	-0.89	+0.69	+0.79	+0.96	+0.99
IPSL-CM6A-LR	62	+0.77	+0.74	+0.77	-0.51	-0.45	+0.17	+0.57	+0.60	+0.91
MPI-ESM1-1-2-HAM	54	+0.49	+0.34	+0.08	-0.18	+0.20	-0.01	+0.15	+0.62	+0.56
MPI-ESM1-2-HR	64	+0.71	+0.85	+0.78	-0.79	-0.74	-0.40	-0.35	+0.58	+0.72
MPI-ESM1-2-LR	63	+0.51	+0.58	+0.35	-0.42	-0.19	-0.07	-0.05	+0.67	+0.58
MRI-ESM2-0	62	+0.88	+0.90	+0.88	-0.64	-0.52	-0.01	+0.23	+0.65	+0.88
NorCPM1	58	+0.96	+0.86	+0.92	-0.55	-0.63	+0.56	+0.53	+0.97	+0.97
UKESM1-0-LL	62	+0.88	+0.88	+0.73	-0.83	-0.71	+0.75	+0.85	+0.74	+0.96

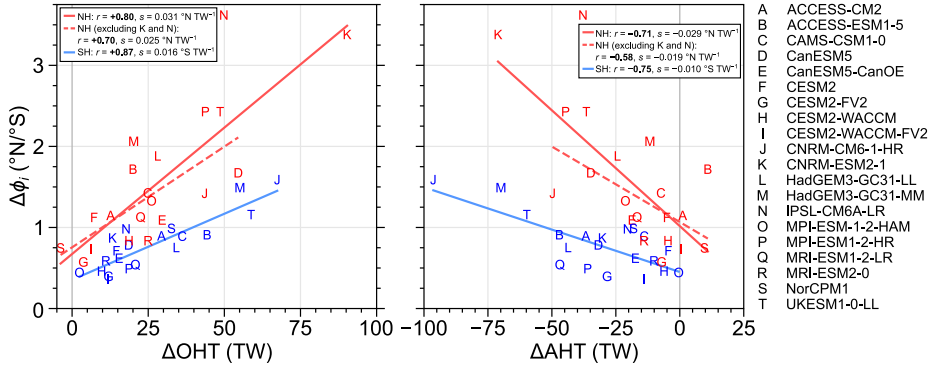


Fig. 4 Maximum increase in 25-year mean $\Delta\phi_t$, plotted against the corresponding change in poleward (left) OHT and (right) AHT. Heat transports are here evaluated at 65°N/S. Red points are Northern Hemisphere (NH) and blue points are Southern Hemisphere (SH). Ordinary least-squares regression lines are added to all models for the NH (red, solid); excluding models K and N (red, dashed); and to all models for the SH (blue, solid). The legends give the corresponding correlation coefficients (r) and slopes of the regression lines (s). 1 TW = 10¹² W

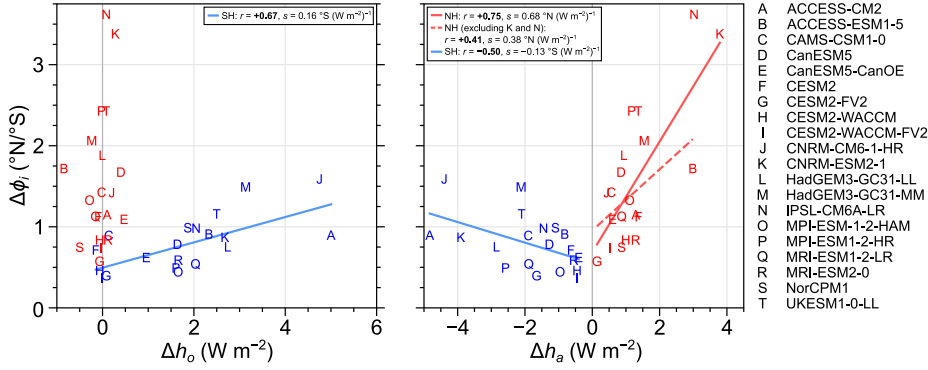


Fig. 5 As in Fig. 4 but for (left) OHT convergence averaged over sea ice (h_o) and (right) AHT convergence averaged over sea ice (h_a)

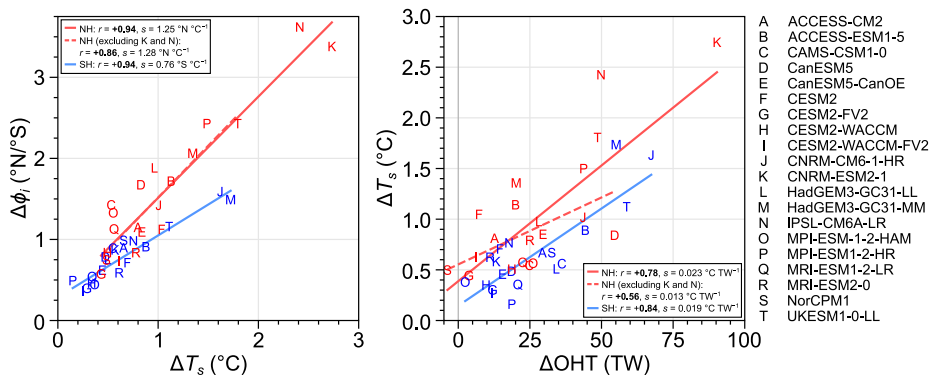


Fig. 6 As in Figs. 4 and 5 but for (left) ϕ_i and mean near-surface air temperature, T_s , and (right) T_s and OHT. Here, OHT is evaluated at 65°N/S and T_s is averaged between 65°N/S and the pole

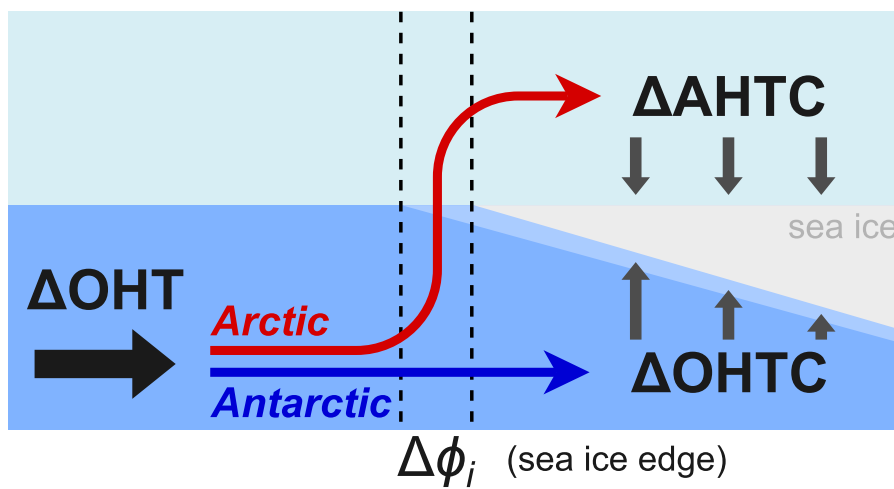


Fig. 7 Schematic summary of the mechanisms of OHT influence on the sea ice edge (ϕ_i) inferred from CMIP6 PI-control analysis

4 Discussion and conclusions

In this paper, we analysed the response of Arctic and Antarctic sea ice extent to natural fluctuations in OHT occurring in the PI-control simulations of 20 CMIP6 models. A summary of our key findings is as follows:

1. Arctic and Antarctic sea ice extent contracts with increased poleward OHT, with significant correlation in all models.
2. In the northern hemisphere, for most models:
 - (a) the direct effect of OHT is concentrated convergence and melting at the ice edge in the Atlantic sector;
 - (b) there is no substantial role of OHTC in the central Arctic;
 - (c) a secondary Arctic-wide ice thinning occurs, mediated by increased high-latitude AHTC.
3. In the southern hemisphere, for most models:
 - (a) the effect of OHT is relatively-uniform convergence and consequent melting under the entire Antarctic ice pack;
 - (b) AHT does not have a direct impact on the ice cover, but transports some ocean heat away from the ice pack.

The difference between Arctic and Antarctic sea ice behaviours is summarised by Figs. 4 and 5: the former emphasises point (1), similarly to Mahlstein and Knutti (2011) for CMIP3 in the NH, while the latter shows our main novel result—that OHT takes different ‘pathways’ in each hemisphere (see also Fig. 7). From Fig. 4a we can also infer that Arctic sea ice is about twice as sensitive to poleward OHT than Antarctic sea ice, although there are caveats in this statement—it depends on the choice of reference latitude, and the cross-model behaviour does not necessarily reflect individual model behaviours. Regardless, the change of slope between hemispheres in Fig. 4a likely reflects the difference in mechanism, since local OHTC along the ice edge in the North Atlantic is several times larger than OHTC under the Antarctic ice pack (Figs. 2–3), even though Δ OHT is similar for HadGEM3-GC31-LL in both hemispheres (Fig. 4a). It is worthwhile to note that Aylmer et al. (2020) show that OHTC concentrated near the sea ice edge is about twice as effective at shrinking the ice cover as the equivalent OHTC averaged over the ice pack in an idealised energy balance model, thus mimicking the behaviour of the comprehensive GCMs shown here.

Our study adds to the growing evidence that OHT is a key player in the long-term evolution of sea ice extent, and our results are generally consistent with previous work. In particular, the effect of OHT being concentrated near the ice edge in the Atlantic sector has been noted in individual model sensitivity studies (see section 1). Our analysis shows this relationship exists within simulated unforced climate variability. Furthermore, we provide evidence for the robustness of this relationship across models.

We acknowledge that our study has limitations. Although using PI-control simulations means that our results are not dependent on a forced response, a disadvantage is that some models have quite small magnitudes of internal variability, which hides the signal of the effect of OHT on sea ice behind noise. Analysing a large sample of GCMs comes at the cost of it being impractical to analyse every detail of the simulations; for example, we did not consider ice dynamics. This could be relevant to both Arctic sea ice (e.g. as in Castruccio et al., 2019, who suggest a dynamic response of Arctic sea ice to atmospheric circulation changes) and Antarctic sea ice (e.g. Sun and Eisenman, 2021, showing improved comparison of simulated to observed trends after manually correcting Antarctic sea ice drift in CESM). The thermodynamic interpretations we have put forward are not called into question by this,

431 but the role of dynamics would make a worthwhile future study as this could point to a
432 specific area of model improvement for sea ice simulation.

433 Why does OHT continue under and through sea ice in the SH but is lost nearer the
434 ice edge in the NH? Our study does not provide the tools to rigorously answer this, but an
435 explanation could be presumed based on current understanding of the Arctic and Southern
436 Oceans in today's climate. In the central Arctic, sea ice is thick and high in concentration,
437 preventing ocean–atmosphere exchanges, and the upper ocean is stably stratified, prevent-
438 ing heat release from Atlantic inflow (Carmack et al., 2015). This probably explains why
439 OHTC—roughly the air–sea flux—does not change in the central Arctic in the PI-control
440 simulations. In the Southern Ocean, the mean sea ice concentration is relatively low, such
441 that ocean heat loss is less restricted. Whatever the reasons, the fact that robustly-different
442 behaviours are exhibited in the NH and SH indicates different approaches for tackling Arctic
443 and Antarctic sea ice uncertainties.

444 While some studies have assessed the role of OHT in future sea ice loss (section 1),
445 to our knowledge none have investigated quantitatively the relevance to intermodel spread
446 or applied such analyses to plausible emission scenario simulations. Mahlstein and Knutti
447 (2011) show significant anticorrelation between Arctic sea ice extent historical simulations
448 and OHT across CMIP3 models—indirectly, Fig. 5 suggests this is the case for CMIP6. In
449 light of persistent intermodel spread and extensive evidence for the impact of OHT on sea
450 ice, a multi-model investigation into OHT changes and projected rates of sea ice loss could
451 help constrain future estimates by identifying sources of uncertainty and possible areas for
452 model improvement.

453 **Acknowledgements** The corresponding author is funded by the Natural Environment Research Council
454 (NERC) via the SCENARIO Doctoral Training Partnership (NE/L002566/1). We acknowledge the World
455 Climate Research Programme, which, through its Working Group on Coupled Modelling, coordinated and
456 promoted CMIP6. We thank the climate modelling groups for producing and making available their model
457 output, the Earth System Grid Federation (ESGF) for archiving the data and providing access, and the multiple
458 funding agencies who support CMIP6 and ESGF.

459 **Compliance with ethical standards**

460 **Data availability** Raw CMIP6 data is publicly accessible from the ESGF data nodes. The processed data is
461 available upon reasonable request from the lead author (see also below regarding code availability).

462 **Code availability** Python code used to compute diagnostics in this study are available on GitHub at <https://github.com/jakeaylmer/cmip-diagnostics>.

464 **Conflict of interest** The authors declare that they have no conflict of interest.

465 **References**

- 466 Auclair G, Tremblay LB (2018) The role of ocean heat transport in rapid sea ice declines
467 of the Community Earth System Model Large Ensemble. *J Geophys Res* 123:8941–8957,
468 doi:[10.1029/2018JC014525](https://doi.org/10.1029/2018JC014525)
- 469 Aylmer J, Ferreira D, Feltham D (2020) Impacts of oceanic and atmospheric heat transports
470 on sea ice extent. *J Climate* 33:7197–7215, doi:[10.1175/JCLI-D-19-0761.1](https://doi.org/10.1175/JCLI-D-19-0761.1)

- 471 Bi D, Dix M, Marsland S, O'Farrell S, Sullivan A, Bodman R, et al. (2020) Configuration
472 and spin-up of ACCESS-CM2, the new generation Australian Community Climate and
473 Earth System Simulator Coupled Model. *Journal of Southern Hemisphere Earth Systems
474 Science* 70:225–251, doi:[10.1071/ES19040](https://doi.org/10.1071/ES19040)
- 475 Bitz CM, Holland MM, Hunke EC, Moritz RE (2005) Maintenance of the Sea-Ice Edge. *J
476 Climate* 18:2903–2921, doi:[10.1175/JCLI3428.1](https://doi.org/10.1175/JCLI3428.1)
- 477 Bjerknes J (1964) Atlantic air-sea interaction. *Advances in Geophysics* 10:1–82,
478 doi:[10.1016/S0065-2687\(08\)60005-9](https://doi.org/10.1016/S0065-2687(08)60005-9)
- 479 Boucher O, Servonnat J, Albright AL, Aumont O, Balkanski Y, Bastrikov V, et al. (2020)
480 Presentation and evaluation of the IPSL-CM6A-LR climate model. *J Adv Model Earth
481 Syst* 12:e2019MS002010, doi:[10.1029/2019MS002010](https://doi.org/10.1029/2019MS002010)
- 482 Budikova D (2009) Role of Arctic sea ice in global atmospheric circulation: A review.
483 *Global and Planetary Change* 68:149–163, doi:[10.1016/j.gloplacha.2009.04.001](https://doi.org/10.1016/j.gloplacha.2009.04.001)
- 484 Carmack E, Polyakov I, Padman L, Fer I, Hunke E, Hutchings J, et al. (2015) Toward quan-
485 tifying the increasing role of oceanic heat in sea ice loss in the new Arctic. *Bull Am
486 Meteorol Soc* 96:2079–2105, doi:[10.1175/BAMS-D-13-00177.1](https://doi.org/10.1175/BAMS-D-13-00177.1)
- 487 Castruccio FS, Ruprich-Robert Y, Yeager SG, Danabasoglu G, Msadek R, Delworth TL
488 (2019) Modulation of Arctic sea ice loss by atmospheric teleconnections from Atlantic
489 Multidecadal Variability. *J Climate* 32:1419–1441, doi:[10.1175/JCLI-D-18-0307.1](https://doi.org/10.1175/JCLI-D-18-0307.1)
- 490 Convey P, Peck LS (2019) Antarctic environmental change and biological responses. *Sci
491 Adv* 5:eaz0888, doi:[10.1126/sciadv.aaz0888](https://doi.org/10.1126/sciadv.aaz0888)
- 492 Counillon F, Keenlyside N, Bethke I, Wang Y, Billeau S, Shen ML, Bentsen M (2016) Flow-
493 dependent assimilation of sea surface temperature in isopycnal coordinates with the Nor-
494 wegian Climate Prediction Model. *Tellus A: Dynamic Meteorology and Oceanography*
495 68:32437, doi:[10.3402/tellusa.v68.32437](https://doi.org/10.3402/tellusa.v68.32437)
- 496 Danabasoglu G, Lamarque JF, Bacmeister J, Bailey DA, DuVivier AK, Edwards J, et al.
497 (2020) The Community Earth System Model Version 2 (CESM2). *J Adv Model Earth
498 Syst* 12:e2019MS001916, doi:[10.1029/2019MS001916](https://doi.org/10.1029/2019MS001916)
- 499 Ding Q, Scheiger A, L'Heureux M, Battisti DS, Po-Chedley S, Johnson NC, et al. (2017)
500 Influence of high-latitude atmospheric circulation changes on summertime Arctic sea ice.
501 *Nat Clim Change* 7:289–295, doi:[10.1038/nclimate3241](https://doi.org/10.1038/nclimate3241)
- 502 Docquier D, Koenigk T, Fuentes-Franco R, Karami MP, Ruprich-Robert Y (2021) Impact of
503 ocean heat transport on the Arctic sea-ice decline: a model study with EC-Earth3. *Clim
504 Dyn* 56:1407–1432, doi:[10.1007/s00382-020-05540-8](https://doi.org/10.1007/s00382-020-05540-8)
- 505 Eisenman I (2010) Geographic muting of changes in the Arctic sea ice cover. *Geophysical
506 Research Letters* 37, doi:[10.1029/2010GL043741](https://doi.org/10.1029/2010GL043741)
- 507 Eisenman I (2012) Factors controlling the bifurcation structure of sea ice retreat. *J Geophys
508 Res* 117, doi:[10.1029/2011JD016164](https://doi.org/10.1029/2011JD016164)
- 509 Ferreira D, Marshall J, Rose BEJ (2011) Climate Determinism Revisited: Multiple Equilibria
510 in a Complex Climate Model. *J Climate* 24:992–1012, doi:[10.1175/2010JCLI3580.1](https://doi.org/10.1175/2010JCLI3580.1)
- 511 Ferreira D, Marshall J, Ito T, McGee D (2018) Linking Glacial–Interglacial states to multiple
512 equilibria of climate. *Geophys Res Lett* 45:9160–9170, doi:[10.1029/2018GL077019](https://doi.org/10.1029/2018GL077019)
- 513 Koenigk T, Brodeau L (2014) Ocean heat transport into the arctic in the twentieth and
514 twenty-first century in EC-Earth. *Clim Dyn* 42:3101–3120, doi:[10.1007/s00382-013-
515 1821-x](https://doi.org/10.1007/s00382-013-1821-x)
- 516 Mahlstein I, Knutti R (2011) Ocean Heat Transport as a Cause for Model Uncertainty in
517 Projected Arctic Warming. *J Climate* 24:1451–1460, doi:[10.1175/2010JCLI3713.1](https://doi.org/10.1175/2010JCLI3713.1)
- 518 Mauritsen T, Bader J, Becker T, Behrens J, Bittner M, Brokopf R, et al. (2019) Developments
519 in the MPI-M Earth System Model version 1.2 (MPI-ESM1.2). *J Adv Model Earth Syst*

- 11:998–1038, doi:[10.1029/2018MS001400](https://doi.org/10.1029/2018MS001400)
- 520 Meier WN, Hovelsrud GK, Oort BEH, Key JR, Kovacs KM, Michel C, et al. (2014) Arctic
521 sea ice in transformation: A review of recent observed changes and impacts on biology
522 and human activity. *Rev Geophys* 52:185–217, doi:[10.1002/2013RG000431](https://doi.org/10.1002/2013RG000431)
- 523 Menary MB, Kuhlbrodt T, Ridley J, Andrews MB, Dimdore-Miles OB, Deshayes J, et al.
524 (2018) Preindustrial Control Simulations With HadGEM3-GC3.1 for CMIP6. *J Adv*
525 *Model Earth Syst* 10:3049–3075, doi:[10.1029/2018MS001495](https://doi.org/10.1029/2018MS001495)
- 526 Müller WA, Jungclaus JH, Mauritsen T, Baehr J, Bittner M, Budich R, et al. (2018)
527 A Higher-Resolution Version of the Max Planck Institute Earth System Model (MPI-
528 ESM1.2-HR). *J Adv Model Earth Syst* 10:1383–1413, doi:[10.1029/2017MS001217](https://doi.org/10.1029/2017MS001217)
- 529 Notz D, Marotzke J (2012) Observations reveal external driver for arctic sea-ice retreat.
530 *Geophys Res Lett* 39:L08502, doi:[10.1029/2012GL051094](https://doi.org/10.1029/2012GL051094)
- 531 Notz D, SIMIP Community (2020) Arctic sea ice in CMIP6. *Geophys Res Lett*
532 46:e2019GL086749, doi:[10.1029/2019GL086749](https://doi.org/10.1029/2019GL086749)
- 533 Nummelin A, Li C, J HP (2017) Connecting ocean heat transport changes from the midlati-
534 tudes to the Arctic Ocean. *Geophys Res Lett* 44:1899–1908, doi:[10.1002/2016GL071333](https://doi.org/10.1002/2016GL071333)
- 535 Parkinson CL (2019) A 40-y record reveals gradual Antarctic sea ice increases followed by
536 decreases at rates far exceeding the rates seen in the Arctic. *Proc Natl Acad Sci* 29:14414–
537 14423, doi:[10.1073/pnas.1906556116](https://doi.org/10.1073/pnas.1906556116)
- 538 Poulsen CJ, Jacob RL (2004) Factors that inhibit snowball Earth simulation. *Paleoceanog-*
539 *raphy* 19:PA4021, doi:[10.1029/2004PA001056](https://doi.org/10.1029/2004PA001056)
- 540 Roach LA, Dörr J, Holmes CR, Massonnet F, Blockley EW, Notz D, Rackow T, Raphael
541 MN, O’Farrell SP, Bailey DA, Bitz CM (2020) Antarctic sea ice area in CMIP6. *Geophys*
542 *Res Lett* 47:e2019GL086729, doi:[10.1029/2019GL086729](https://doi.org/10.1029/2019GL086729)
- 543 Rong X, Li J, Chen H, Xin Y, Su J, Hua L, et al. (2018) The CAMS Climate System Model
544 and a Basic Evaluation of Its Climatology and Climate Variability Simulation. *Journal of*
545 *Meteorological Research* 32:839–861, doi:[10.1007/s13351-018-8058-x](https://doi.org/10.1007/s13351-018-8058-x)
- 546 Rose BEJ (2015) Stable “Waterbelt” climates controlled by tropical ocean heat transport:
547 A nonlinear coupled climate mechanism of relevance to Snowball Earth. *J Geophys Res*
548 120:1404–1423, doi:[10.1002/2014JD022659](https://doi.org/10.1002/2014JD022659)
- 549 Rose BEJ, Marshall J (2009) Ocean heat transport, sea ice, and multiple cli-
550 mate states: Insights from energy balance models. *J Atmos Sci* 66:2828–2843,
551 doi:[10.1175/2009JAS3039.1](https://doi.org/10.1175/2009JAS3039.1)
- 552 Rosenblum E, Eisenman I (2017) Sea ice trends in climate models only accurate in runs
553 with biased global warming. *J Climate* 30:6265–6278, doi:[10.1175/JCLI-D-16-0455.1](https://doi.org/10.1175/JCLI-D-16-0455.1)
- 554 Séférian R, Nabat P, Michou M, Saint-Martin D, Voldoire A, Colin J, et al. (2019) Eval-
555 uation of CNRM Earth System Model, CNRM-ESM2-1: Role of Earth System Pro-
556 cesses in Present-Day and Future Climate. *J Adv Model Earth Syst* 11:4182–4227,
557 doi:[10.1029/2019MS001791](https://doi.org/10.1029/2019MS001791)
- 558 Sellar AA, Jones CG, Mulcahy JP, Tang Y, Yool A, Wiltshire A, et al. (2019) UKESM1:
559 Description and Evaluation of the U.K. Earth System Model. *J Adv Model Earth Syst*
560 11:4513–4558, doi:[10.1029/2019MS001739](https://doi.org/10.1029/2019MS001739)
- 561 Simpkins GR, Ciasto LM, Thompson DWJ, England MH (2012) Seasonal Relationships
562 between Large-Scale Climate Variability and Antarctic Sea Ice Concentration. *J Climate*
563 25:5451–5469, doi:[10.1175/JCLI-D-11-00367.1](https://doi.org/10.1175/JCLI-D-11-00367.1)
- 564 Singh HA, Rasch PJ, Rose BEJ (2017) Increased Ocean Heat Convergence Into the High
565 Latitudes With CO₂ Doubling Enhances Polar-Amplified Warming. *Geophysical Re-*
566 *search Letters* 44:10583–10591, doi:[10.1002/2017GL074561](https://doi.org/10.1002/2017GL074561)
- 567

- 568 Sun S, Eisenman I (2021) Observed Antarctic sea ice expansion reproduced in a
569 climate model after correcting biases in sea ice drift velocity. *Nat Commun* 12,
570 doi:[10.1038/s41467-021-21412-z](https://doi.org/10.1038/s41467-021-21412-z)
- 571 Swart NC, Cole JNS, Kharin VV, Lazare M, Scinocca JF, Gillett NP, et al. (2019) The Can-
572 dian Earth System Model version 5 (CanESM5.0.3). *Geoscientific Model Development*
573 12:4823–4873, doi:[10.5194/gmd-12-4823-2019](https://doi.org/10.5194/gmd-12-4823-2019)
- 574 Voltaire A, Saint-Martin D, Sénési S, Decharme B, Alias A, Chevallier M, et al. (2019)
575 Evaluation of CMIP6 DECK Experiments With CNRM-CM6-1. *J Adv Model Earth Syst*
576 11:2177–2213, doi:[10.1029/2019MS001683](https://doi.org/10.1029/2019MS001683)
- 577 Winton M (2003) On the climatic impact of ocean circulation. *J Climate* 16:2875–2889,
578 doi:[10.1175/1520-0442\(2003\)016<2875:OTCIOO>2.0.CO;2](https://doi.org/10.1175/1520-0442(2003)016<2875:OTCIOO>2.0.CO;2)
- 579 Yukimoto S, Kawai H, Koshiro T, Oshima N, Yoshida K, Urakawa S, et al. (2019) The
580 Meteorological Research Institute Earth System Model Version 2.0, MRI-ESM2.0: De-
581 scription and Basic Evaluation of the Physical Component. *Journal of the Meteorological*
582 *Society of Japan* 97:931–965, doi:[10.2151/jmsj.2019-051](https://doi.org/10.2151/jmsj.2019-051)
- 583 Ziehn T, Chamberlain MA, Law RM, Lenton A, Bodman RW, Dix M, et al. (2020) The Aus-
584 tralian Earth System Model: ACCESS-ESM1.5. *Journal of Southern Hemisphere Earth*
585 *Systems Science* 70:193–214, doi:[10.1071/ES19035](https://doi.org/10.1071/ES19035)

Supplementary Files

This is a list of supplementary files associated with this preprint. Click to download.

- [aylmer2021SM1.pdf](#)
- [aylmer2021SM2.pdf](#)